

Article

Histogram Matching of Sentinel-2 Spectral Information to Enhance Planetscope Imagery for Effective Wildfire Damage Assessment

Minho Kim  · Minyoung Jung  · Yongil Kim  [†]

Abstract: In abrupt fire disturbances, high quality images suitable for wildfire damage assessment can be difficult to acquire. Quantifying wildfire burn area and severity are essential measures for quick short-term disaster response and efficient long-term disaster restoration. Planetscope (PS) imagery offers 3 m spatial and daily temporal resolution, which can overcome the spatio-temporal resolution tradeoff of conventional satellites, albeit at the cost of spectral resolution. This study investigated the potential of augmenting PS imagery by integrating the spectral information from Sentinel-2 (S2) differenced Normalized Burn Ratio (dNBR) to PS differenced Normalized Difference Vegetation Index (dNDVI) using histogram matching, specifically for wildfire burn area and severity assessment of the Okgye wildfire which occurred on April 4th, 2019. Due to the difficulty in acquiring reference data, the results of the study were compared to the wildfire burn area reported by Ministry of the Interior and Safety. The burn area estimates from this study demonstrated that the histogram-matched (HM) PS dNDVI image produced more accurate burn area estimates and more descriptive burn severity intervals in contrast to conventional methods using S2. The HM PS dNDVI image returned an error of only 0.691% whereas the S2 dNDVI and dNBR images overestimated the wildfire burn area by 5.32% and 106%, respectively. These improvements using PS were largely due to the higher spatial resolution, allowing for the detection of sparsely distributed patches of land and narrow roads, which were indistinguishable using S2 dNBR. In addition, the integration of spectral information from S2 in the PS image resolved saturation effects in areas of low and high burn severity.

Key Words: Burn area, Okgye-myeon Wildfire, Planetscope, Sentinel-2, Histogram Matching

1. Introduction

Accurate quantification of burned area and detailed discrimination of burn severity are paramount to

implement prompt disaster response measures in the short-term and to promote efficient restoration of the local environment in the long-term. Conventional methods such as field surveying were typically

Received July 28, 2019; Revised August 3, 2019; Accepted August 16, 2019; Published online August 21, 2019

¹⁾ Master Student, Department of Civil and Environmental Engineering, Seoul National University

²⁾ PhD Student, Department of Civil and Environmental Engineering, Seoul National University

³⁾ Professor, Department of Civil and Environmental Engineering, Seoul National University

[†] Corresponding Author: Yongil Kim (yik@snu.ac.kr)

This is an Open-Access article distributed under the terms of the Creative Commons Attribution Non-Commercial License (<http://creativecommons.org/licenses/by-nc/3.0>) which permits unrestricted non-commercial use, distribution, and reproduction in any medium, provided the original work is properly cited.

expensive and slow. In contrast, satellite imagery provides crucial information of the Earth's surface at lower costs, higher temporal frequency, wider spatial coverage, and faster processing speed over conventional methods.

Although optical sensors are influenced by cloud coverage and atmospheric conditions, they yield reasonably accurate damage assessment results. Recent studies in literature revealed that medium-resolution optical satellite imagery such as Landsat-8 Operational Land Imager/Thermal Infrared Sensor (OLI/TIRS) and Sentinel-2 (S2) MultiSpectral Instrument (MSI) were used most frequently for this purpose (Fernández-García *et al.*, 2017; Navarro *et al.*, 2017; Sobrino *et al.*, 2019). Very High Resolution (VHR) satellite sensors such as Worldview-2 (Meng *et al.*, 2017) and Geoeye-1 (Dragozi *et al.*, 2016) offer sub-meter spatial resolution and outstanding image quality, but at longer revisit times and higher costs. Satellites with high temporal resolution such as Moderate Resolution Imaging Spectroradiometer (MODIS) (Levin and Heimowitz, 2012) and Himawari-8 (Jang *et al.*, 2019) are available, but are restricted by their coarse spatial resolution. As can be inferred from the shortcomings of these various sensors, optical satellite sensors suffer from an inevitable trade-off between spatial and temporal resolution.

The recent emergence of nanosatellite technology has unveiled a cost-effective solution with the potential to finally overcome this spatio-temporal limitation (Houborg and McCabe, 2016; Houborg and McCabe, 2018a; Houborg and McCabe, 2018b). At the forefront of this development is Planet Labs as the global, commercially-leading provider using Planetscope (PS), a constellation of more than 120 Cubesats. PS uses one Near-Infrared (NIR) and three visible (VIS) bands at 3 m spatial resolution to supply daily global coverage in a sun-synchronous orbit at 475 km altitude and International Space Station (ISS) orbit at 400 km altitude. The Cubesats are lightweight and inexpensive,

consisting of essentially a multispectral sensor and downlinking system (Cooley *et al.*, 2017).

PS offers an alternative solution to this aforementioned trade-off issue by providing shorter revisit times, higher spatial resolution, reasonable pricing of satellite imagery, and sufficient coverage of the damaged site. However, previous studies using PS have focused on burn area estimation or burn severity assessment using limited levels of classification. For instance, one recent study conducted wildfire damage classification in wildland-urban forest regions, but the results were restricted to using only VIS-NIR spectral information due to the limited number of spectral bands (Michael *et al.*, 2018). Moreover, there is yet no universal standard for classifying wildfire burn severity using VIS-NIR images. This study therefore presents the prospect of exploiting the high spectral resolution of optical satellites and high spatial-temporal resolution of PS. Histogram matching, or histogram specification, is utilized in order to combine the information from the different sensors, without permanently changing the image itself. This method is particularly useful if high quality ground truth data or conventionally used optical satellite images are not available for wildfire burn area and severity assessment.

This study is organized in the following order: Section 2 introduces the study area and gives a descriptive overview of the datasets used to investigate the Okgye-myeon wildfire. Section 3 presents the overall methodology and supporting concepts to this research such as spectral indices and differential images used in wildfire damage assessment. Section 4 shows the results of the wildfire damage assessment through the analysis of burn area and severity. Lastly, the conclusion provides a summative review of the study and closing remarks on the potential of PS for both short- and long-term wildfire damage assessment.

2. Study Area and Datasets

1) Study Area:

Okgye-myeon, Gangwon Province

The wildfire was discovered on April 4th, 2019 at 23:46 Korean Standard Time (KST), south of Okgye-myeon in Gangwon province. Based on a rural household survey conducted by the Korean Statistical Information Service in 2018, Okgye-myeon is a small, rural town with a population of 4,089 and a population density of 27.5 person/km². Subsequent investigations revealed that the fire was triggered by sparks from electrical wires and the wildfire expanded rapidly due to the arid climate, high leaf area, distribution of low-moisture coniferous trees, and high wind velocity (Ministry of the Interior and Safety, 2019). According to the disaster response and recovery report issued by Ministry of the Interior and Safety (MOIS) on April 18th, 2019, the Okgye-myeon wildfire scorched 714.8 ha, resulting in one casualty and damaging multiple buildings, facilities, and equipment (MOIS, 2019). The study area used in this research is displayed in Fig. 1 using a PS image taken a day before the wildfire outbreak.

2) Datasets

In this study, PS images were mainly used for damage assessment of the Okgye wildfire. PS imagery is provided in three product types: Level-1B Basic scene, Level-3A Visual/Analytic ortho-scene, and Level-3B Visual/Analytic ortho-tile. Level-3 products are geometrically and radiometrically corrected images that are ready for further analysis. Despite the high spatio-temporal resolution however, due to the limited number of PS bands and its broad, overlapping spectral bandwidths, S2 images were used to integrate high spectral resolution information for more effective wildfire damage assessment. S2 data were selected given the sensor's extensive spectral range, narrow bandwidths, reliable radiometric characteristics, accessibility of free data, reasonable revisit time, and similar spatial resolution in comparison to PS imagery. Basic specifications of the two satellites are shown in Table 1 and the spectral resolutions of the two sensors are plotted together in Fig. 2.

In general, previous studies claimed that PS images suffer from poor radiometric resolution, low signal-to-noise ratio, and cross-sensor inconsistencies (Cooley *et al.*, 2017; Houborg and McCabe, 2018a; Houborg and

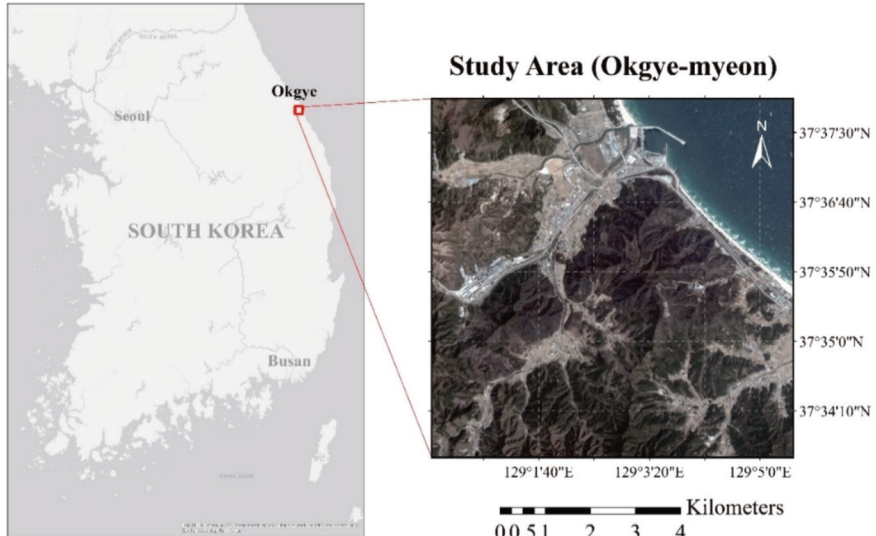


Fig. 1. Study area of Okgye-myeon using PS imagery taken on April 3rd, 2019.

Table 1. Specifications of PS and S2 satellite imagery

Specifications	PS	S2
Operator	Planet Labs	European Space Agency (ESA)
Spatial resolution	3.7 m (At nadir)	10 m (VIS-NIR), 20 m (SWIR and Red-edge), 60 m (Other)
Spectral resolution	4 bands	13 bands
Temporal resolution	Daily	5 days

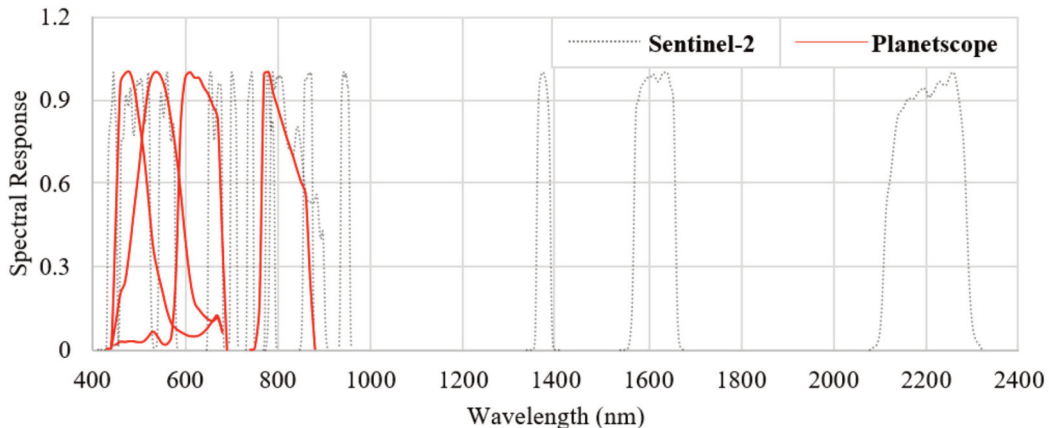


Fig. 2. Comparison of spectral response functions between S2 MSI and PS.

McCabe, 2018b). In response to these issues, Planet Labs processes PS image acquisitions using various types of corrections and calibration/validation procedures. In-house correction methods include pre-launch and on-orbit sensor calibration, rigorous orthorectification using fine DEM and bundle adjustment algorithm, and mosaicking of acquired image stitches (Cooley *et al.*, 2017; Cooley *et al.*, 2019; Houborg and McCabe, 2016; Houborg and McCabe, 2018b; Sadeh *et al.*, 2019). Since this research is focused on post-processing the acquired PS images for wildfire damage assessment,

Level-3 Analytic PS ortho-scene images were selected to minimize preprocessing steps. Images were selected based on minimal cloud coverage, sun zenith angle, revisit time, and overall scene quality. The detailed specifications of the datasets used in this study are listed in Table 2. Multiple PS images were acquired because the coverage of a single image was too small to cover the entire wildfire.

Table 2. Specifications of input datasets used for wildfire damage assessment

Sensor	Acquisition Time (year/month/date)	Sensor Type	Spatial Resolution	Cloud Coverage (%)		
PS	19/04/03 (Top)	Flock-3P-68 (Dove 1004) Launched: Feb. 15, 2017	3 m (VIS-NIR)	0.0		
	19/04/03 (Bottom)					
	19/04/08 (Top)	Flock-3P-77 (Dove 0F28) Launched: Feb. 15, 2017				
	19/04/08 (Bottom)					
S2	19/04/03	S2A	10 m (VIS-NIR) 20 m (SWIR)	3.0		
	19/04/08	S2B		2.5		

3. Methodology

The workflow of this study and the following sections from 3.1 to 3.4 are illustrated below in Fig. 3.

1) Preprocessing

(1) Preprocessing of S2 Images

The S2 images were processed using a common architecture for Sentinel toolboxes called Sentinels Application Program (SNAP) version 6.0. The first step for preprocessing was to correct the input images to Level-2 products using Sen2Cor by ESA. This module performs atmospheric, terrain, and cirrus correction of Top of Atmosphere (TOA) from a Level-1C input image to generate Level-2A surface reflectance products (Louis *et al.*, 2016). Second, band resampling

was processed to match the different spatial resolutions of S2's spectral bands as shown in Table 1. Third, unnecessary water bodies and noise values were masked from the image. This filtering step was processed by using the Normalized Difference Water Index (NDWI) (McFeeters, 1996) where, in general, values greater than zero indicate the presence of water or moisture.

$$\text{NDWI} = \frac{\text{Green} - \text{NIR}}{\text{Green} + \text{NIR}} \quad (1)$$

Normalized Difference Vegetation Index (NDVI) is also considered during this step, where values less than zero are regarded as non-vegetation. Lastly, the images were re-projected to the Universal Transverse Mercator (UTM) 52N coordinate system and fitted according to a subset of the wildfire region.

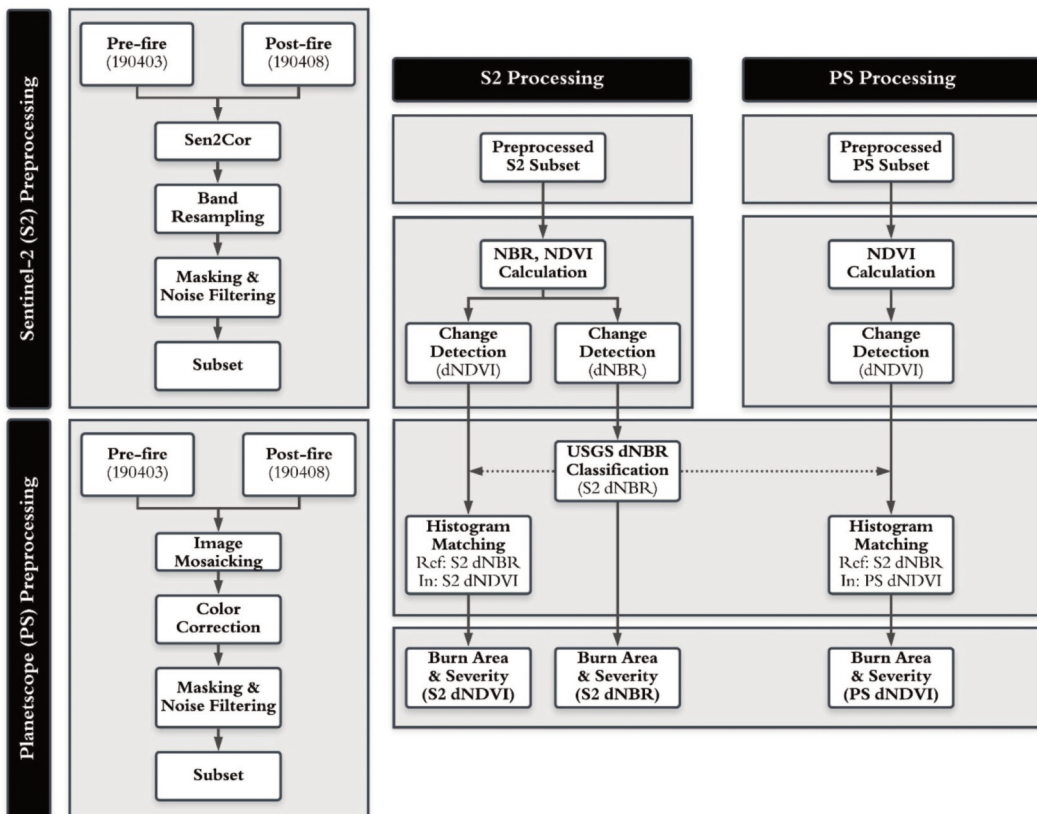


Fig. 3. Conceptual diagram of wildfire damage assessment in terms of burn area and severity mapping, where "Ref" and "In" denote the reference and input images used for histogram matching, respectively.

(2) Preprocessing of PS Images

Additional preprocessing of the images is necessary even after Planet Lab's rigorous corrections and calibration/validation procedures. For this study, the PS images were processed using the image analysis software, Environment for Visualizing Images (ENVI) version 5.3. First, two ortho-scene products are required for full coverage of the wildfire. Since the images were acquired from different PS sensors, seamless image mosaicking and color correction of the images are needed. Noisy data and water bodies should then be filtered prior to analysis. Lastly, the images are re-projected and fitted to the subset area.

PS band correlation is evaluated provided its sensors possess broad and overlapping spectral response functions (refer to Fig. 2). Previous studies claimed that the NIR band held weak or non-existent correlation with VIS bands, especially for scenes which included water bodies (Wicaksono and Lazuardi, 2018). This correlation is significant because the NIR band can be used to remove noise pixels such as sun glint in homogenous water bodies. The relationship between NIR and Red bands can be assessed using regression analysis to ensure effective masking of the images. The ensuing masking and subset steps were conducted in a similar manner to that of S2.

2) Spectral Indices for Wildfire Damage Assessment

The evaluation of burn area and severity via remote sensing methods in literature can be divided into three types of methods (Brewer *et al.*, 2005; Fernández-García *et al.*, 2018): image transformation approaches such as spectral mixture analysis (Fernández-Manso *et al.*, 2009; Quintano *et al.*, 2013) and tasseled cap transformation (Fornacca *et al.*, 2018); radiative transfer models (Chuvieco *et al.*, 2006); and spectral indices (Fornacca *et al.*, 2018; Fernández-García *et al.*, 2018; Sobrino *et al.*, 2019; Fernández-Manso *et al.*,

al., 2016). Among these approaches, spectral indices are effective for wildfire damage assessment because of their computationally light and relatively accurate performance. Despite the diversity of spectral indices available, there is yet no consensus on the most optimal and robust index for wildfire damage assessment (Cansler and McKenzie, 2012; Fernández-García *et al.*, 2018). NDVI has been used often in the past to evaluate wildfire damage because the index can accentuate the spectral characteristics of vegetation and non-vegetation (including burned areas) at NIR and red bands. More recently, Normalized Burn Ratio (NBR) (Key and Benson, 2003) has become one of the most commonly-used and adopted indices for the detection of wildfire burn scars (Henry, 2008; Kontoes *et al.*, 2009) and burn severity (Cocke *et al.*, 2005; Escuin *et al.*, 2008). NBR utilizes the contrasting response of short-wave infrared (SWIR) and NIR bands reflected between burned areas and healthy vegetation. The two spectral ratios are given by the following band combinations:

$$\text{NDVI} = \frac{\text{NIR} - \text{RED}}{\text{NIR} + \text{RED}} \quad (2)$$

$$\text{NBR} = \frac{\text{NIR} - \text{SWIR}}{\text{NIR} + \text{SWIR}} \quad (3)$$

NBR is particularly effective because the SWIR band adds another dimension to sense wildfire burn damage (Fornacca *et al.*, 2018; Fernández-García *et al.*, 2018; Sobrino *et al.*, 2019). Common issues when using these spectral indices include the saturation of NBR in severely burned areas (Fernández-García *et al.*, 2018).

3) Generation of Differential Images

In the short-term aftermath of a sudden wildfire outbreak, a single post-fire image processed using optimal spectral indices can suffice to produce a glimpse of the wildfire damage for rapid disaster response (Lentile *et al.*, 2006). However, post-fire

Table 3. Summary of spectral indices used for wildfire damage assessment

Spectral Index	PS	Spatial Resolution	S2	Spatial Resolution
NDVI	$\frac{\text{band}_4 - \text{band}_3}{\text{band}_4 + \text{band}_3}$	3 m	$\frac{\text{band}_8 - \text{band}_4}{\text{band}_8 + \text{band}_4}$	10 m
NBR	—	—	$\frac{\text{band}_8 - \text{band}_{12}}{\text{band}_8 + \text{band}_{12}}$	20 m

images with minimal cloud coverage, favorable weather conditions, and full scene coverage may not be available in the first place. In this case, mono-temporal analysis using a single image can cause confusion when interpreting features which exhibit similar spectral characteristics, such as shadows and burned areas (Viana-Soto *et al.*, 2017). The present study focused on the bi-temporal analysis of spectral ratio images, similar to change detection, but used only the differential images to minimize the effect of shadows and to manipulate the spectral characteristics of burned areas with surrounding features such as vegetation and bare soil. In comparison to the mono-temporal spectral ratio method mentioned above, the analysis of differential images of pre- and post-fire images enabled more accurate assessment of the wildfire burn area and severity. Detailed information of the spectral indices used in this study are listed in Table 3 with respect to their corresponding S2 and PS input datasets.

To create a differential image, the difference in NBR (dNBR) and difference in NDVI (dNDVI) between pre- and post-fire images are calculated using the expressions:

$$\text{dNBR} = \text{NBR}_{\text{pre}} - \text{NBR}_{\text{post}} \quad (4)$$

$$\text{dNDVI} = \text{NDVI}_{\text{pre}} - \text{NDVI}_{\text{post}} \quad (5)$$

Previous studies on dNBR by the United States Geological Survey (USGS) developed a burn severity classification standard presented in Table 4 (Key and Benson, 2003; Key and Benson, 2006). The dNBR intervals have been used widely in wildfire damage research (Cocke *et al.*, 2005; Miller and Thode, 2007;

Table 4. Burn severity in terms of dNBR (USGS Classification Standard)

dNBR	Burn Severity
< -0.25	High post-fire regrowth
-0.25 to -0.1	Low post-fire regrowth
-0.1 to +0.1	Non-burn
0.1 to 0.27	Low-severity burn
0.27 to 0.44	Moderate-low (Mod-low) severity burn
0.44 to 0.66	Moderate-high (Mod-high) severity burn
> 0.66	High-severity burn

Sobrino *et al.*, 2019), but there is yet no common wildfire burn severity classification scheme available for NDVI or NIR-based indices. One particular study using PS images quantified wildfire damage in three levels of burn severity (Michael *et al.*, 2018). However, VIS-NIR based spectral indices can be inadequate to yield informative results for accurate wildfire damage assessment.

4) Integration of Spectral Information

In order to transfer S2 spectral information to the high spatial resolution PS image, this study performed histogram matching of the two images, provided that the images reflected similar characteristics for wildfire damage assessment. Histogram matching, also referred to as histogram specification, is defined as matching the pixel value distribution from a reference image, denoted as P_R , to an input image, denoted as P_A , by using a mapping function which describes the transfer of pixel values along the spatial domain (Gonzalez and Woods, 2002). In principle, histogram matching is based on computing the cumulative distributions for each image and mapping the input image's value at a

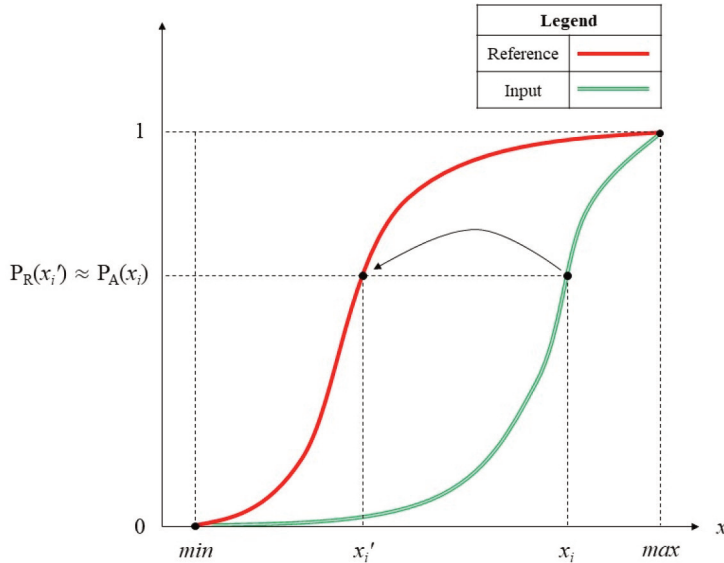


Fig. 4. Conceptual example of histogram matching values from input to reference datasets.

given threshold point to the reference value that has the same probability. This procedure is displayed by the plot in Fig. 4. When converting to the histogram-matched (HM) image, the value of $P_A(x_i)$ is found where the reference and input images are related such that:

$$P_A(x_i) \approx P_R(x_i) \quad (6)$$

Based on this threshold value, x_i is allocated to its new position x_i' on the input image histogram. The matching procedure can be expressed by a combination of the two distribution functions as:

$$x_i' = P_R^{-1} P_A(x_i) \quad (7)$$

The result is the HM image $P_{A'}$ which contains information from the reference image's domain mapped on the input image's domain.

In this study, histogram matching of the spectral index images was processed using SNAP. The S2 dNBR reference was formed by initially grading the distribution according to the intervals specified in the USGS dNBR classification scheme in Table 4. S2 dNDVI and PS dNDVI were used as input images with

S2 dNBR as the reference image to generate two HM images.

4. Results and Discussion

1) Preprocessing

(1) Preprocessing Results of S2 Images

Two S2 datasets were generated at spatial resolutions of 20 m and 10 m for NBR and NDVI computations, respectively. NDWI values greater than zero were considered as water bodies and masked to reduce the effect of noise on the image.

(2) Preprocessing Results of PS Images

The top and bottom scenes for both pre- and post-fire images were mosaicked using edge feathering and seam interpolation. The mosaicked image was color-corrected to compensate for the difference in tone between the two scenes. Next, prior to filtering water bodies, the correlation between NIR and VIS bands was evaluated.

The noise filtering process for the PS images was

executed in a similar manner to the S2 images. Preprocessed results displayed in Fig. 5(c) and (d) demonstrated an increase in correlation between the NIR and Red bands, thus signifying the water bodies

as significant noise sources which can decrease the radiometric quality of PS images. Further to the analysis of Fig. 5, high NIR values at low Red band values (around 500) were caused by abnormally large

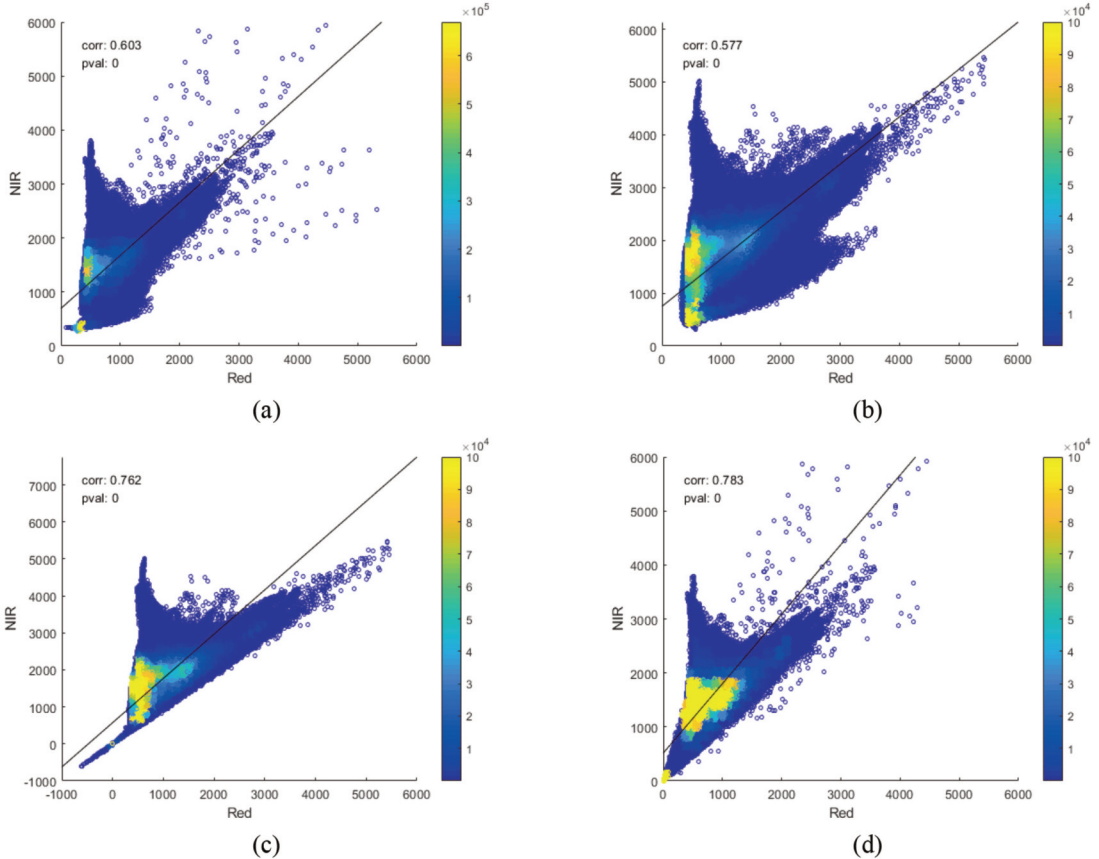


Fig. 5. Regression analysis of PS NIR and Red bands. (a) Pre-fire image (19/04/03); (b) Post-fire image (19/04/08); (c) Pre-fire image with water bodies filtered; (d) Post-fire image with water bodies filtered.

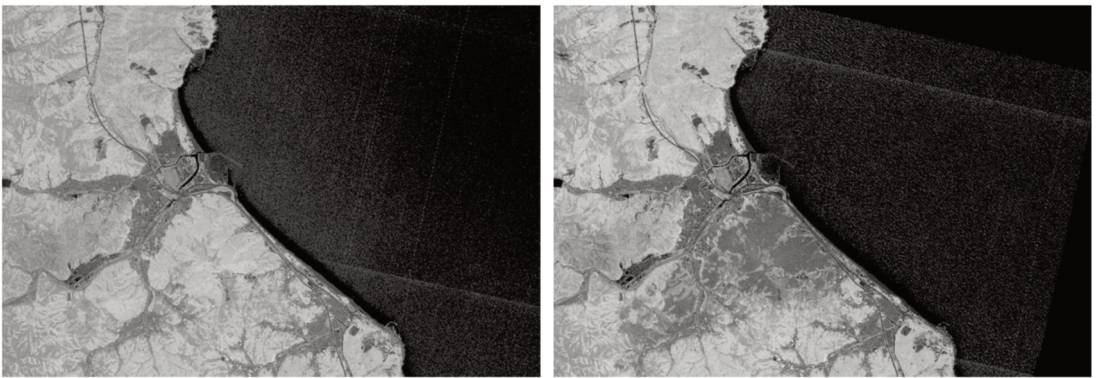


Fig. 6. Noise streaks stretching across both land and water areas in pre-fire (left) and post-fire (right) PS NDVI images calculated prior to preprocessing (to accentuate noise streaks).

Table 5. Regression analysis results of correlation values following masking of water bodies

Masking	Pre-fire (19/04/03)	Post-fire (19/04/08)
Water not masked	0.603	0.577
Water masked	0.762	0.783

reflectance values from highly reflective building and roof materials. In addition, noise streaks were observed in the NDVI and NDWI calculations of both pre- and post-fire images, as depicted in Fig. 6, which can ultimately increase the margin of error in burn area and severity assessment. Correlation coefficient values found by regression analysis between the NIR and Red bands are summarized in Table 5. This study revealed that the masking of water bodies was able to increase the correlation values of the pre- and post-fire images to enhance image quality for subsequent processing. This result is in accordance to the aforementioned study by Wicaksono and Lazuardi (2018) which noted the low correlation between NIR and VIS bands.

2) Generation of Differential Images

The S2 dNBR, S2 dNDVI, and PS dNDVI differential images are displayed as grayscale images in Fig. 7. The right-side of the S2 post-fire image (19/04/08) was missing because full coverage of the wildfire burn area was unavailable. In addition, the PS result was

able to differentiate small-sized patches and narrow areas due to its high spatial resolution. This advantage proved to be significant in performing more accurate burn area estimation and is discussed in more detail in Section 4.4.

3) Integration of Spectral Information

Prior to histogram matching, the feasibility of transferring spectral information across the histogram distributions of the two sensors was evaluated to ensure reliable representation of features in both images. Regression analysis can be used for preliminary evaluation of the correlation between the calculated spectral index images. In this study, regression analysis was conducted for three sets of data. First, S2 dNBR and S2 dNDVI were compared in order to assess the relationship between different spectral indices. Second, S2 dNDVI and PS dNDVI were compared to evaluate the degree of similarity when using the same spectral index with two different sensors. Third, the S2 dNDVI and S2 dNBR were compared to compute the correlation of using different sensors and spectral indices.

S2 dNBR (20 m resolution) was resampled and matched with S2 dNDVI (10 m resolution) at 20 m resolution. Regression analysis of the two images revealed a very high correlation coefficient of 0.980 between dNBR and dNDVI as shown in Fig. 8(a).

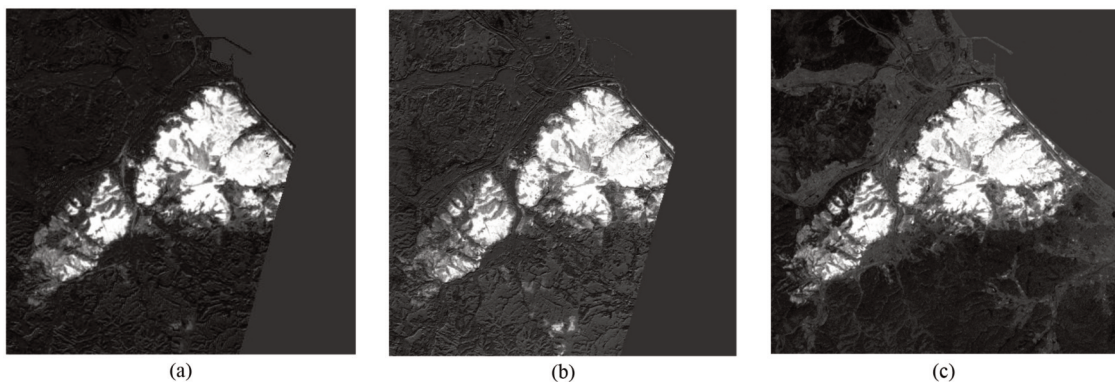


Fig. 7. Differential spectral index images prior to burn severity classification shown in grayscale. (a) S2 dNBR (20 m resolution); (b) S2 dNDVI (10 m resolution); (c) PS dNDVI (3 m resolution).

This result was expected since both images were based on acquisitions from the same sensor, and since the indices are sensitive to similar responses in the spectral characteristics of vegetation and non-vegetation. Second, the S2 dNDVI (10 m resolution) was resampled and matched with PS dNDVI (3 m resolution) at 10 m resolution. Despite the difference between the locations of the two spectral response functions (refer to Fig. 2), the two dNDVI images returned a relatively high correlation coefficient of 0.900 as displayed in Fig. 8(b). Lastly, the PS dNDVI (3 m resolution) was resampled and matched with S2 dNBR at 20 m resolution. As presented in Fig. 8(c), the regression result of both images yielded a higher correlation coefficient of 0.930 in comparison to that of the S2 and PS regression

Table 6. Summary of correlation coefficients from regression analysis of differential images

Compared Images for Regression Analysis		Correlation Coefficient
S2 dNBR	S2 dNDVI	0.980
S2 dNDVI	PS dNDVI	0.900
S2 dNBR	PS dNDVI	0.930

analysis in Fig. 8(b). Based on the overall high level of correlation coefficients found in each regression analysis (refer to Table 6), this study was able to assume the feasibility of using S2 and PS images for histogram matching.

Upon further inspection of Fig. 8(b), S2 dNDVI values of zero can be seen rising vertically along the PS dNDVI axis because of the missing portion in the

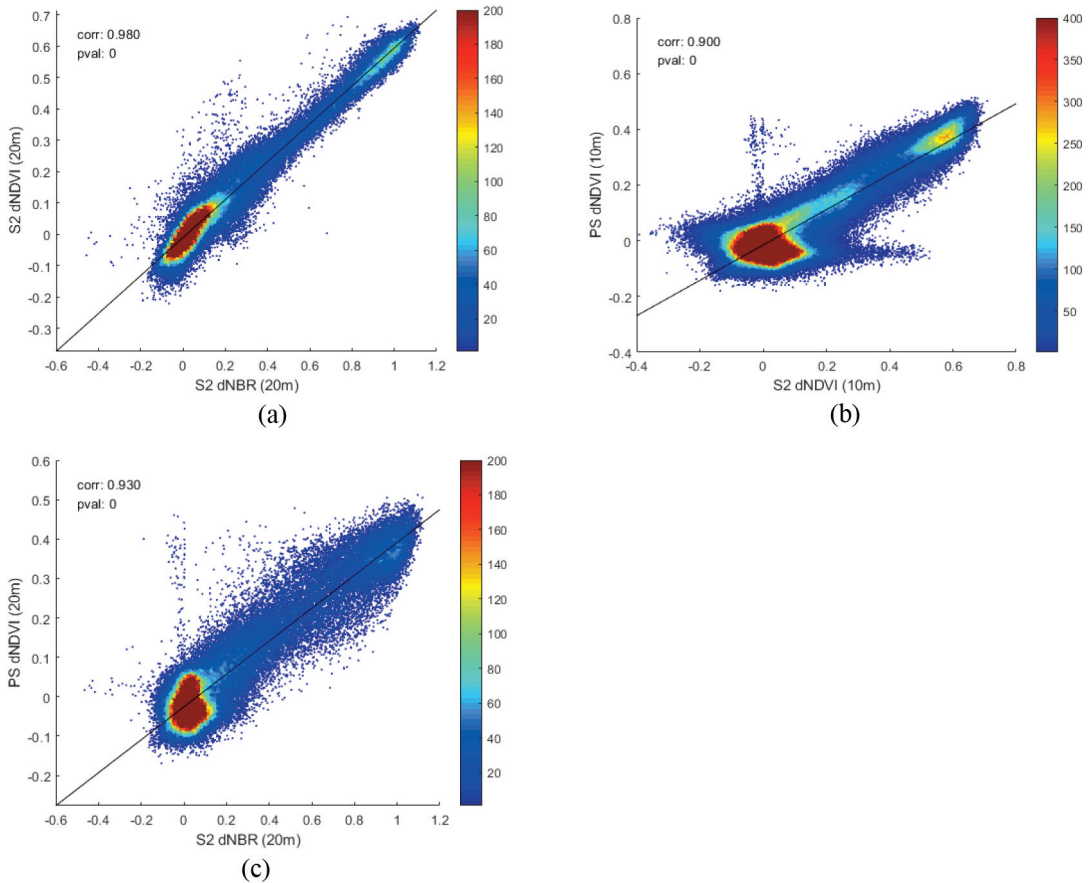


Fig. 8. Correlation prior to histogram matching. (a) S2 dNBR (20 m) with S2 dNDVI (20 m resampled); (b) S2 dNDVI (10 m) with PS dNDVI (10 m resampled); (c) S2 dNBR (20 m) with PS dNDVI (20 m resampled).

S2 post-fire image. PS dNDVI values of zero stretch horizontally along the S2 dNDVI axis due to the presence of clouds in the S2 image. Furthermore, each regression plot in Fig. 8 consists of two concentrated regions of high point density. Based on the thresholds specified in Table 4 and considering the correlation values found through regression analysis, this study assumed that the dNBR thresholds were related to the dNDVI intervals. For instance, given dNBR values of zero indicate no change over time, values less than or greater than 0.2 are likely to show a decrease or increase in vegetation distribution, respectively.

Stemming from this assumption, the first concentrated region is located near zero within an approximate range of -0.2 to +0.2, while the second region is situated at higher values of the compared images. The first region was determined to be rural residential areas and non-vegetation terrain since these areas typically display minimal or no change over time. The first region can

thus be found in similar ranges for each plot in Fig. 8. On the other hand, the range of values of the second region varied for each plot in Fig. 8, which was expected due to the difference in spectral indices and sensors of the input images. These regions of high values were considered to be pixels from the burned area since the eradication of vegetation by the wildfire can be attributed to the steep decrease in spectral response before and after the fire. In more detail, while the high density region, assumed to be burned area in Fig. 8(a), appeared symmetric and evenly distributed along the regression line with respect S2 dNBR and dNDVI, the points of higher density in Fig. 8(b) tended to be concentrated in the PS image. Accordingly, PS dNDVI results should reflect the burned areas better than S2 dNDVI results at higher dNDVI values.

The S2 dNBR image was first classified for burn severity using Table 4. For histogram matching the classified S2 dNBR result was used as the reference

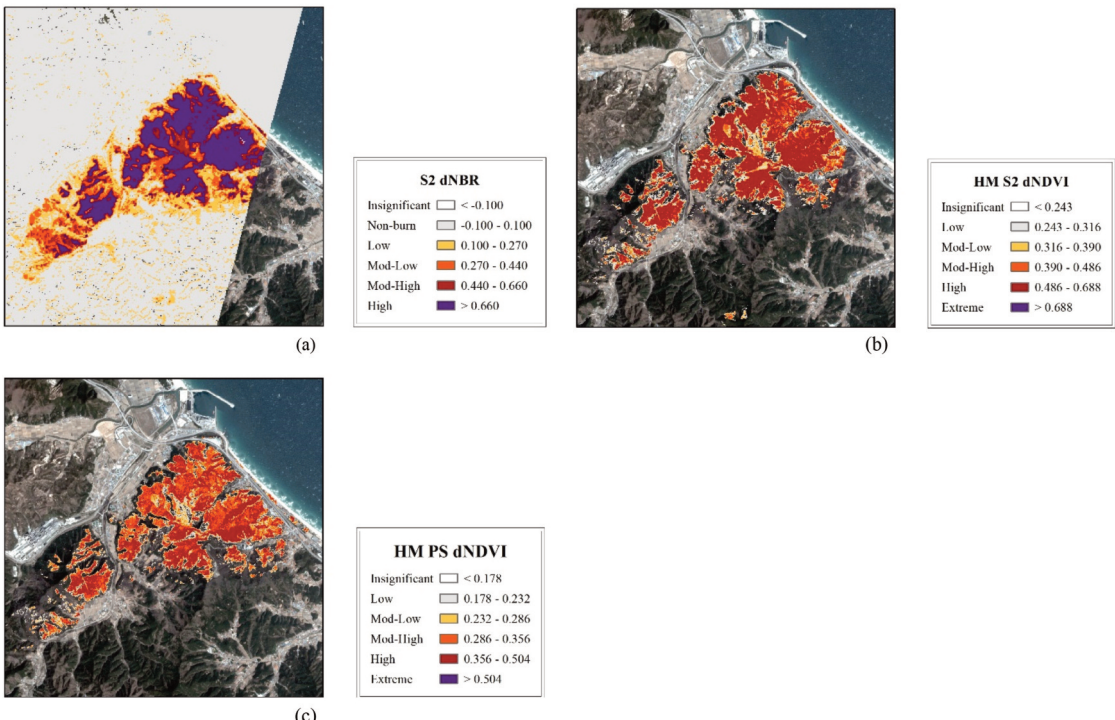


Fig. 9. Burn severity results presented over the PS post-fire (19/04/08) basemap image. (a) S2 dNBR classified using Table 4; (b) HM S2 dNDVI; (c) HM PS dNDVI.

image while S2 dNDVI and PS dNDVI results were used as the input images. The burn severity intervals of “regrowth” were not specified and were naturally included in the “non-burn” interval in order to focus on burned areas. Using the image’s minimum and maximum pixel values as boundary thresholds, six intervals were used to classify S2 dNBR for burn severity. The resulting image and the burn severity intervals are presented in Fig. 9(a), while the HM S2 dNDVI and HM PS dNDVI results are displayed with their corresponding burn severity intervals in Fig. 9(b) and (c), respectively. The effect of histogram matching alleviated the high concentration of data in the reference image’s saturated “high” burn severity interval, particularly due to its relatively broad range (0.660 to maximum value). Moreover, the “non-burn” and “low” intervals of the reference image were better distributed in the HM images. Based on visual analysis of the HM results, the “non-burn” interval was discarded and the “extreme” interval was added for abnormally high values. This shift in intervals, following histogram matching, generated a more descriptive interpretation burn severity and more accurate burn area estimate for both HM images.

4) Wildfire Damage Assessment: Burn Area and Burn Severity

Burn area and severity of the three images in Fig. 9 were calculated and are presented in Table 7 to Table 9. For the S2 dNBR result, provided in Table 7, the overall burned area of 1,472.4 ha far exceeded the reference area of 714.8 ha. This overestimation of 106% was assumed to be caused by the saturation effects at high burn severity values (> 0.66) and the inability of S2 dNBR to differentiate actual burned areas at lower severity levels (0.1 – 0.27 and 0.27 – 0.44). The HM S2 dNDVI result, shown in Table 8, produced a much more respectable estimate at 752.80 ha, only overestimating the reference value by 5.32%. The drawback however is that this overestimation error

is actually larger if the missing portion of the S2 image and the misclassified clouds in the bottom of the image were to be considered. Taking into account this margin of error, the HM PS dNDVI result, given in Table 9, produced the most accurate estimate at 709.86, only underestimating the reference burned area value by 0.691%.

Previous studies have also noted saturation effects of dNBR in regions of high burn severity, which can be the result of a combination of error sources. First, S2 dNBR was not able to differentiate burned area with

Table 7. Wildfire damage assessment of S2 dNBR in terms of burn severity intervals based on Table 4

Interval	Category	# Pixels	Area (ha)
< 0.100	No burn	91,489	3,659.56
0.100-0.270	Low	13,962	558.48
0.270-0.440	Mod-Low	5,956	238.24
0.440-0.660	Mod-High	4,232	169.28
0.660-1.200	High	12,660	506.40
> 1.200	Extreme	0	0
Total Burned (Low-Extreme)		22,848	1,472.40

Table 8. Wildfire damage assessment of HM S2 dNDVI in terms of burn severity

Interval	Category	# Pixels	Area (ha)
< 0.243	No burn	566,312	5663.12
0.243-0.316	Low	14,425	144.25
0.316-0.390	Mod-Low	9,687	96.87
0.390-0.486	Mod-High	12,049	120.49
0.486-0.688	High	39,100	391.00
> 0.688	Extreme	19	0.19
Total Burned (Low-Extreme)		75,280	752.80

Table 9. Wildfire damage assessment of HM PS dNDVI in terms of burn severity

Interval	Category	# Pixels	Area (ha)
< 0.178	Non-burn	6,297,509	5667.76
0.178-0.232	Low	135,732	122.16
0.232-0.286	Mod-Low	115,302	103.77
0.286-0.356	Mod-High	250,643	225.58
0.356-0.504	High	286,855	258.17
> 0.504	Extreme	203	0.18
Total Burned (Low-Extreme)		788,735	709.86

narrow roads (Fig. 10(b) and Fig. 12(b)) and sparsely distributed patches of bare soil (Fig. 11(b)), likely due to the sensor's coarse spatial resolution. Second, as suggested by the overestimation of low-burn severity, the utilization of the USGS classification scheme on S2 dNBR was determined to be unsuitable for use in this area of South Korea. Third, shadows and mountainous terrain nearby may have influenced the detection of burned area. In contrast to S2 dNBR, both HM results

were able to distinguish non-vegetation such as narrow roads (Fig. 10(c) and (d)) and small patches of bare soil (Fig. 11(c) and (d)) effectively. Between the two HM results, HM PS dNDVI was able to detect small patches more accurately given its higher spatial resolution. Furthermore, the HM results were not overwhelmed by saturation effects at high burn severity, and were therefore able to differentiate between the low burn and high burn severity more effectively. With regards to the

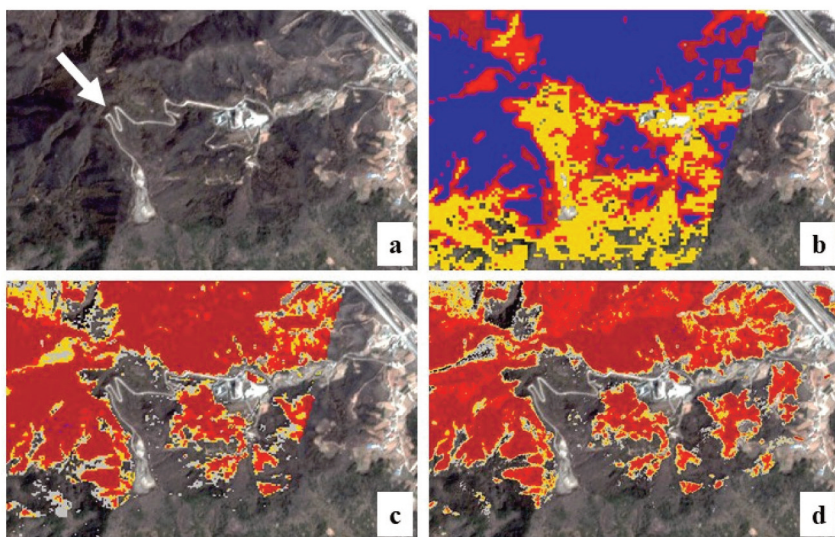


Fig. 10. Close-up images depicting narrow roads within mountainous region.

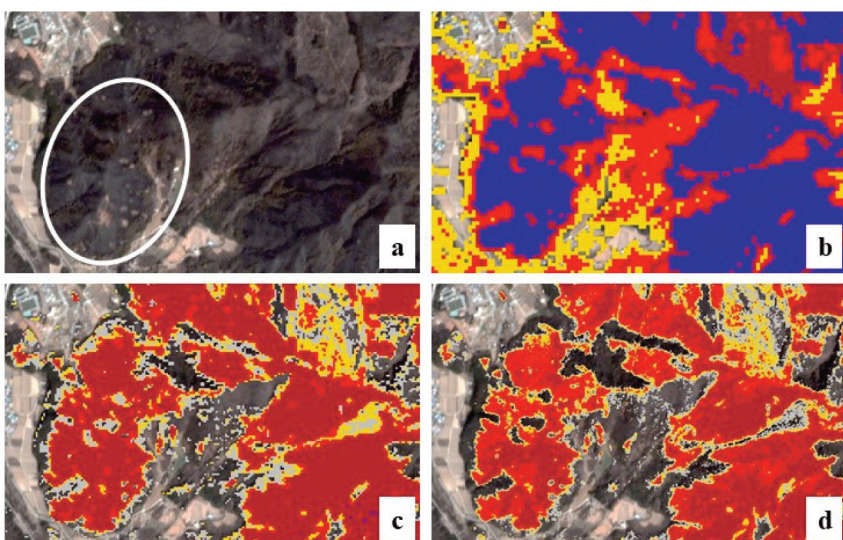


Fig. 11. Close-up images showing small, sparsely-distributed patches of bare soil.

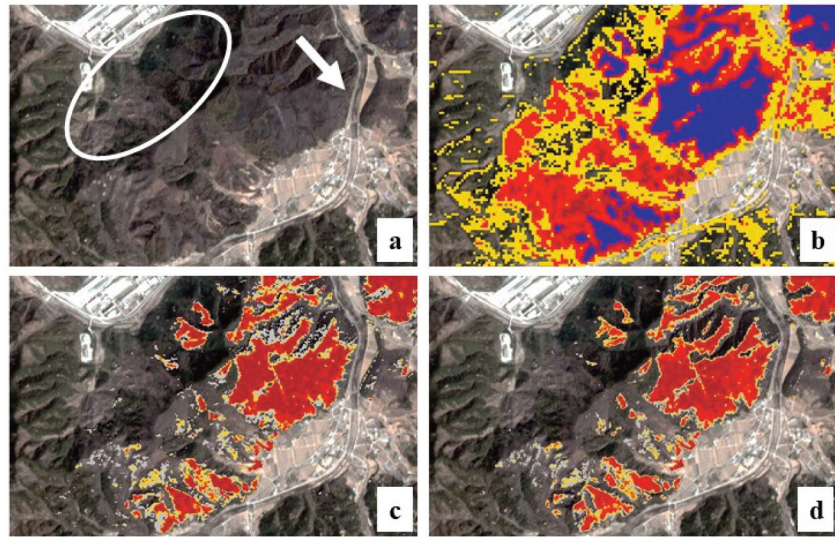


Fig. 12. Close-up images of burned area in mountainous terrain undetected by HM results.

two HM results, HM PS dNDVI displayed less saturation at “Mod-High” and “High” intervals of burn severity. Nevertheless, there were some regions where the HM results were not able to classify. While S2 dNBR successfully recognized this burned area, as shown in Fig. 12(b), the HM results were only able to classify nearby regions of high burn severity in Fig. 12(c) and (d). This margin of error demonstrated that dNDVI is more susceptible to topographic variation and shadows in comparison to dNBR when detecting regions of low burn severity. Noise streaks revealed in Fig. 6 and noise pixels in the image can compound to the error in the HM PS result as well.

Overall, the HM PS dNDVI exhibited the highest precision in delineating narrow roads and detecting small patches of bare soil sparsely-distributed within and nearby the burned area. Close-up images of these features are provided in Fig. 10 to Fig. 12 in order to highlight the advantage of HM PS dNDVI’s high spatial resolution in comparison to the other results. From Fig. 10 to Fig. 12, (a) is a subset of the post-fire (19/04/08) Planetscope image and is also used as a basemap for the other images (b) to (d), where (b) is the S2 dNBR burn severity result, (c) is the HM S2

dNDVI burn severity result, and (d) is the HM PS dNDVI burn severity result. Noteworthy features are indicated using white arrows and circles on image (a).

5. Conclusion

In this study, damage assessment of the Okgye-myeon wildfire, in terms of evaluating the burn area and severity, was processed using differential S2 and PS images of pre and post-fire NDVI calculations using spectral information transferred from S2 dNBR via histogram matching. Burn severity calculated by the HM PS dNDVI result generated the most accurate estimate of burned area of 709.86 ha (in comparison to the reference value of 714.8 ha as per MOIS) and detailed assessment of the Okgye-myeon wildfire burn severity. This research determined the importance of combining high spatial and spectral resolution in an effort to improve the mapping quality of wildfire burn area and severity. The results highlighted that PS imagery can overcome the spatio-temporal resolution trade-off to process high quality burn area and severity images quickly and accurately for short-term rapid

disaster response and long-term damage mapping and restoration. Since there is yet no global and robust spectral index for burn area and severity mapping, nor a reference classification scheme for burn severity with respect to dNDVI, the results can be used as a preliminary benchmark for wildfire damage assessment.

While PS imagery produced promising results for wildfire damage assessment, this study also observed various lingering problems inherent in the Cubesat imagery. In particular, PS imagery suffered from radiometric and spectral limitations. Noise streaks and color tone difference deteriorated the overall image quality. Future work towards more effective wildfire monitoring and disaster management can include fusion of PS imagery with more highly calibrated satellite sensors to compensate for low SNR and cross-sensor inconsistencies as well as optimal selection of high quality images for more accurate representation of pre- and post-fire data.

Acknowledgements

This research was supported by a grant (2019-MOIS32-015) of Disaster-Safety Industry Promotion Program funded by Ministry of Interior and Safety (MOIS, Korea). Image courtesy of Planet Labs, Inc. Planetscope imagery is provided through the Planet's Education and Research program.

References

- Brewer, C. K., J. C. Winne, R. L. Redmond, D. W. Opitz, and M. V. Mangrich, 2005. Classifying and mapping wildfire severity, *Photogrammetric Engineering and Remote Sensing*, 71(11): 1311-1320.
- Cansler, C. A. and D. McKenzie, 2012. How robust are burn severity indices when applied in a new

region? Evaluation of alternate field-based and remote-sensing methods, *Remote Sensing*, 4(2): 456-483.

Chuvieco, E., D. Riaño, F. M. Danson, and P. Martin, 2006. Use of a radiative transfer model to simulate the postfire spectral response to burn severity, *Journal of Geophysical Research: Biogeosciences*, 111(G4).

Cocke, A. E., P. Z. Fulé, and J. E. Crouse, 2005. Comparison of burn severity assessments using Differenced Normalized Burn Ratio and ground data, *International Journal of Wildland Fire*, 14(2): 189-198.

Cooley, S., L. Smith, L. Stepan, and J. Mascaro, 2017. Tracking dynamic northern surface water changes with high-frequency Planet CubeSat imagery, *Remote Sensing*, 9(12): 1306.

Cooley, S. W., L. C. Smith, J. C. Ryan, L. H. Pitcher, and T. M. Pavelsky, 2019. Arctic-boreal lake dynamics revealed using CubeSat imagery, *Geophysical Research Letters*, 46(4): 2111-2120.

Dragozi, E., I. Z. Gitas, S. Bajocco, and D. G. Stavrakoudis, 2016. Exploring the relationship between burn severity field data and very high resolution GeoEye images: the case of the 2011 Evros wildfire in Greece, *Remote Sensing*, 8(7): 566.

Escuin, S., R. Navarro, and P. Fernandez, 2008. Fire severity assessment by using NBR (Normalized Burn Ratio) and NDVI (Normalized Difference Vegetation Index) derived from LANDSAT TM/ETM images, *International Journal of Remote Sensing*, 29(4): 1053-1073.

Fernández-García, V., M. Santamarta, A. Fernández-Manso, C. Quintano, E. Marcos, and L. Calvo, 2018. Burn severity metrics in fire-prone pine ecosystems along a climatic gradient using Landsat imagery, *Remote Sensing of Environment*, 206: 205-217.

Fernández-Manso, O., C. Quintano, and A. Fernández-

- Manso, 2009. Combining spectral mixture analysis and object-based classification for fire severity mapping, *Forest Systems*, 18(3): 296-313.
- Fernández-Manso, A., O. Fernández-Manso, and C. Quintano, 2016. SENTINEL-2A red-edge spectral indices suitability for discriminating burn severity, *International Journal of Applied Earth Observation and Geoinformation*, 50: 170-175.
- Fornacca, D., G. Ren, and W. Xiao, 2018. Evaluating the best spectral indices for the detection of burn scars at several post-fire dates in a mountainous region of Northwest Yunnan, China, *Remote Sensing*, 10(8): 1196.
- Gonzalez, R. C. and R. E. Woods, 2002. *Digital Image Processing*, Prentice Hall Press, Upper Saddle River, NJ, USA.
- Henry, M. C., 2008. Comparison of single-and multi-date Landsat data for mapping wildfire scars in Ocala National Forest, Florida, *Photogrammetric Engineering and Remote Sensing*, 74(7): 881-891.
- Houborg, R. and M. McCabe, 2016. High-resolution NDVI from Planet's constellation of earth observing nano-satellites: a new data source for precision agriculture, *Remote Sensing*, 8(9): 768.
- Houborg, R. and M. McCabe, 2018a. A Cubesat enabled spatio-temporal enhancement method (CESTEM) utilizing Planet, Landsat and MODIS data, *Remote Sensing of Environment*, 209: 211-226.
- Houborg, R. and M. McCabe, 2018b. Daily retrieval of NDVI and LAI at 3 m resolution via the fusion of CubeSat, Landsat, and MODIS data, *Remote Sensing*, 10(6): 890.
- Jang, E., Y. Kang, J. Im, D. W. Lee, J. Yoon, and S. K. Kim, 2019. Detection and monitoring of forest fires using Himawari-8 geostationary satellite data in South Korea, *Remote Sensing*, 11(3): 271.
- Key, C. H. and N. C. Benson, 2003. *The Normalized Burn Ratio (NBR): A Landsat TM radiometric measure of burn severity*, U.S. Department of the Interior, U.S. Geological Survey, Northern Rocky Mountain Science Center.
- Key, C. H. and N. C. Benson, 2006. Landscape Assessment (LA), In: Lutes, D. C., Keane, R. E., Caratti, J. F., Key, C. H., Benson, N. C., Nathan, C., Sutherland, S., Gangi, L. J. (Ed.), *FIREMON: Fire effects monitoring and inventory system*, General Technical Report RMRS-GTR-164-CD, Fort Collins, CO: US Department of Agriculture, Forest Service, Rocky Mountain Research Station, p. LA-1-55, <https://doi.org/10.2737/RMRS-GTR-164>.
- Kontoes, C. C., H. Poilv  , G. Florsch, I. Keramitsoglou, and S. Paralikidis, 2009. A comparative analysis of a fixed thresholding vs. a classification tree approach for operational burn scar detection and mapping, *International Journal of Applied Earth Observation and Geoinformation*, 11(5): 299-316.
- Lentile, L. B., Z. A. Holden, A. M. Smith, M. J. Falkowski, A. T. Hudak, P. Morgan, S. A. Lewis, P. E. Gessler, and N. C. Benson, 2006. Remote sensing techniques to assess active fire characteristics and post-fire effects, *International Journal of Wildland Fire*, 15(3): 319-345.
- Levin, N. and A. Heimowitz, 2012. Mapping spatial and temporal patterns of Mediterranean wildfires from MODIS, *Remote Sensing of Environment*, 126: 12-26.
- Louis, J., V. Debaecker, B. Pflug, M. Main-Knorn, J. Bieniarz, U. Mueller-Wilm, E. G. Cadau and F. Gascon, 2016. S2 SEN2COR: L2A processor for users, *Proc. of the Living Planet Symposium*, Prague, Czech Republic, May 9-13, pp. 9-13.

- McFeeters, S. K., 1996. The use of the Normalized Difference Water Index (NDWI) in the delineation of open water features, *International Journal of Remote Sensing*, 17(7): 1425-1432.
- Meng, R., J. Wu, K. L. Schwager, F. Zhao, P. E. Dennison, B. D. Cook, K. Brewster, T. M. Green, and S. O. Serbin, 2017. Using high spatial resolution satellite imagery to map forest burn severity across spatial scales in a Pine Barrens ecosystem, *Remote Sensing of Environment*, 191: 95-109.
- Michael, Y., I. Lensky, S. Brenner, A. Tchetchik, N. Tessler, and D. Helman, 2018. Economic assessment of fire damage to urban forest in the wildland-urban interface using Planet satellites constellation images, *Remote Sensing*, 10(9): 1479.
- Miller, J. D. and A. E. Thode, 2007. Quantifying burn severity in a heterogeneous landscape with a relative version of the delta Normalized Burn Ratio (dNBR), *Remote Sensing of Environment*, 109(1): 66-80.
- Ministry of the Interior and Safety, 2019. 20190418 Gangwon East-Sea Irwon wildfire response - recovery report (11AM), https://www.mois.go.kr/frt/bbs/type001/commonSelectBoardArticle.do?bbsId=BBSMSTR_000000000336&nttId=70191, Accessed on Jul. 22, 2019 (in Korean).
- Navarro, G., I. Caballero, G. Silva, P. C. Parra, Á. Vázquez, and R. Caldeira, 2017. Evaluation of forest fire on Madeira Island using S2A MSI imagery, *International Journal of Applied Earth Observation and Geoinformation*, 58: 97-106.
- Quintano, C., A. Fernández-Manso, and D. A. Roberts, 2013. Multiple Endmember Spectral Mixture Analysis (MESMA) to map burn severity levels from Landsat images in Mediterranean countries, *Remote Sensing of Environment*, 136: 76-88.
- Sadeh, Y., X. Zhu, K. Chenu, and D. Dunkerley, 2019. Sowing date detection at the field scale using CubeSats remote sensing, *Computers and Electronics in Agriculture*, 157: 568-580.
- Sobrino, J. A., R. Llorens, C. Fernández, J. M. Fernández-Alonso, and J. A. Vega, 2019. Relationship between soil burn severity in forest fires measured in situ and through spectral indices of remote detection, *Forests*, 10(5): 457.
- Viana-Soto, A., I. Aguado, and S. Martínez, 2017. Assessment of post-fire vegetation recovery using fire severity and geographical data in the Mediterranean region (Spain), *Environments*, 4(4): 90.
- Wicaksono, P. and W. Lazuardi, 2018. Assessment of PS images for benthic habitat and seagrass species mapping in a complex optically shallow water environment, *International Journal of Remote Sensing*, 39(17): 5739-5765.